Investigation of the Avalanche Fluctuations Factor in Time Projection Chamber Detector Using 266 nm UV Laser*

Yue Chang,[1,2] Hui-Rong Qi,[2] Xin She,[2,3] Jin-Xian Zhang,[2,3] Hong-Liang Dai,[2] Chun-Xu Yu,[1] Ling-Hui Wu,[2] Guang Zhao,[2] Jian-Chun Wang,[2] Zhi Deng,[4] Yi-Fang Wang,[2] Yuan-Bo Chen,[2] and Jian Zhang[2]

[1]*School of Physics, Nankai University, Tianjin 300071, China*
[2]*State Key Laboratory of Particle Detection and Electronics (Institute of High Energy Physics, CAS), Beijing 100049, China*
[3]*University of Chinese Academy of Sciences, Beijing 100049, China*
[4]*Department of Engineering Physics, Tsinghua University, Beijing 100084, China*

Time Projection Chambers (TPCs) are extensively used in collider experiments due to their superior physical performance. Particularly for future positron-electron colliders in Higgs physics studies, the next-generation TPC technology must provide better momentum resolution and improved spatial resolution. The avalanche fluctuation factor, a crucial parameter affecting spatial resolution, is challenging to measure accurately, whether directly or indirectly. This research leveraged the exceptional stability and ionization properties of ultraviolet lasers to achieve a precise determination of the avalanche fluctuation factor. The test outcomes were found to agree with the calculated values at the same gain levels, thereby validating the reliability of the experimental findings.

Keywords: Time Projection Chamber, UV laser, Avalanche fluctuation, Gas gain

I. INTRODUCTION

The Time Projection Chamber (TPC) [1] is a gas detector renowned for its high-precision measurements of particle momentum and position, which are crucial for accurate particle identification. Its capabilities have made the TPC a staple in particle physics experiments, as well as in low-energy nuclear physics and the study of double beta decay [2, 4, 5]. The TPC has recently been confirmed as the baseline main track detector in the CEPC [7, 8] Reference Technical Design Report (refTDR). Moreover, the International Linear Collider (ILC) [6]also intends to adopt the TPC as its track detector.

In particular, for Higgs physics research in future positron-electron colliders [11], the next-generation TPC is targeted to achieve a position resolution of approximately 100 μm on tracks that are meters in length. This level of precision is essential to meet the demands for precise physical measurements of Higgs properties. The accuracy of the TPC is heavily dependent on its position resolution, which underscores the importance of measuring and optimizing the parameters that affect this resolution. These parameters are detailed in Eq. (1):

$$\sigma_x^2 = \sigma_0^2 + \frac{D_T^2}{N_{eff}} z + \frac{h^2}{12N_{eff}} \tan^2 \phi \tag{1}$$

The term σ_0 represents the influence of factors such as electronic noise and electron amplification fluctuations on the resolution. The second term accounts for the influence of drift and diffusion on position resolution, which is a primary determinant of the overall resolution. Here, D_T signifies the electron diffusion coefficient, N_{eff} represents the effective number of electrons, and z is the drift distance. The third term addresses the impact of track angles and the pad size on position resolution, with the latter being constrained by N_{eff}. Position resolution is influenced by a multitude of parameters, rendering it a pivotal aspect in the design and optimization of TPCs [12].

The parameters within Eq. (1) can be refined through research on Micro Pattern Gas Detectors, such as GEM [13] and Micromegas [15]. For the CEPC-TPC design, the T2K gas mixture ($Ar:CF_4:iC_4H_{10}$ = 95:3:2) has been chosen as the working gas. This mixture offers a reduced transverse diffusion coefficient, D_T, of approximately $\sim 43\,\mu\text{m}/\sqrt{\text{cm}}$, under the conditions of a 2T magnetic field and an electric field strength of 200 V/cm. This characteristic allows for acceptable resolution degradation even at the maximum drift distance of 290 cm, which is half the length of the CEPC-TPC. However, precise Determining the critical parameter N_{eff} during the initial detector design phase is challenging. This is due to the difficulty in precisely measuring the crucial avalanche fluctuations factor, f, either directly or indirectly. The effective number of electrons, N_{eff}, is delineated by Eq. (2):

$$\frac{1}{N_{eff}} = (1+f)\langle\frac{1}{N}\rangle \tag{2}$$

where N is the average primary ionization count, and $f = (\frac{\sigma_G^2}{\langle G\rangle^2})$ denotes the avalanche fluctuations factor. As the factor f increases, the stability of the gain deteriorates, affecting the position resolution of the detector[18].

In GEM detectors, the factor f represents the gain stability uncertainty due to fluctuations near the micropores, as shown in Fig.1(a). A stable gain is associated with a higher N_{eff} value, ensuring that the induced charge numbers on each pad accurately reflect the primary ionization distribution, thereby yielding precise positional data. In contrast, when gain stability is compromised, as illustrated in the lower section of Fig.1(b), the charge distribution on each pad significantly diverges from the primary ionization. This divergence results

* Supported by the National Natural Science Foundation of China (Grant No.11975256 and No.11775242) and the National Key Research and Development Program of China (No. 2016YFA0400400)

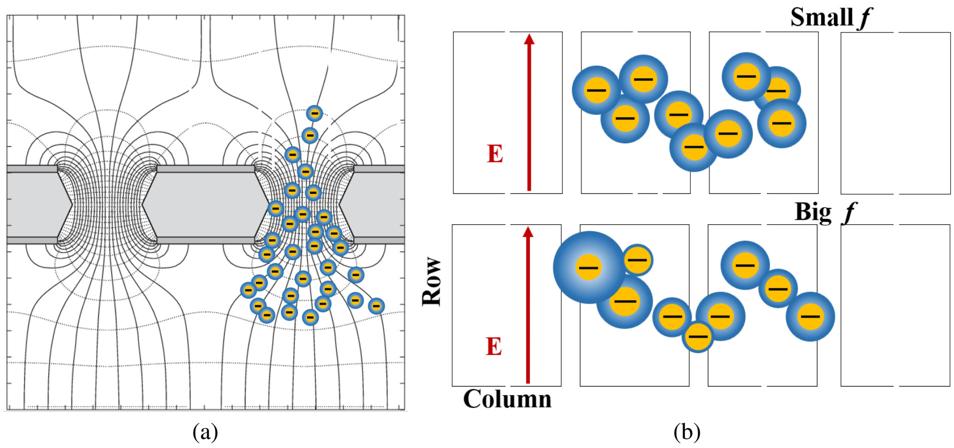

Fig. 1. (a) Schematic diagram of the electric field structure and amplification at the micro-pores of the GEM; (b) The charge distribution on the readout pad of the GEM with the avalanche fluctuation factor f; the upper image represents a schematic diagram for a smaller f, whereas the lower image depicts the outcome for a larger f.

in a diminished N_{eff} value and a consequent degradation in the precision of position information derived from the center-of-gravity method. Consequently, the precise experimental determination of the avalanche fluctuations factor is crucial for optimizing the detector's performance and enhancing its overall precision.

Experimental studies often involve analyzing the gas amplification charge spectrum generated by a single photoelectron from cathode materials. This process is typically facilitated by illuminating materials with LED lamps or lasers to assess avalanche fluctuations. The Micromegas research group at CERN-RD51 has conducted measurements of the factor f using a single-electron approach, achieving a value of $f \sim 0.6$ in a gas mixture of (Ar:iC_4H_{10} = 95:5) [19]. This method is, however, not easy because of electronic noise interference, especially for low gas gains. This degradation complicates measurements, especially when acquisition times are extended and measurement errors are increased. Concurrently, the PandaX collaboration is exploring the factor f utilizing a liquid Xenon TPC [20, 21].

Furthermore, the factor f can be estimated through simulation using empirical formulas, specifically as given in Eq. (3) and Eq. (4).

$$P(G) = C_0 \frac{(1+\theta)^{(1+\theta)}}{\Gamma(1+\theta)} \left(\frac{G}{\langle G\rangle}\right)^{\theta} exp\left[-(1+\theta)\frac{G}{\langle G\rangle}\right] \quad (3)$$

where C_0 is a constant, $\langle G\rangle$ represents the mean gain of the single-electron amplification distribution, and θ is a parameter determining the variance of the Polya distribution[22], which is related to the proportion of electrons with energy exceeding the threshold. The relationship between θ and f is expressed as follows:

$$\theta = \frac{1}{f} - 1 \quad (4)$$

We utilized COMSOL Multiphysics simulation software [23] to model the microstructure of the GEM, which was then imported into Garfield++ [24] for simulating the gain in T2K gas, as depicted in Fig. 2. To align the simulation settings with the experimental conditions, we simulated the distribution of electrons after they had traversed three layers of GEM amplification. By fitting the results with Eq. (3), we obtained the values for C_0, $\langle G\rangle$, and θ, which facilitated the estimation of f using Eq. (4). The simulation outcomes indicate that the value of f is approximately 0.66 with a gain of 1089 in T2K gas.

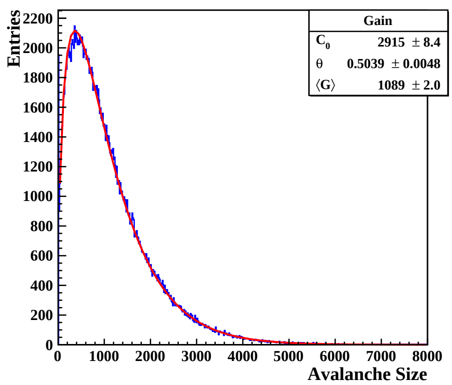

Fig. 2. The electron distribution after Triple-GEM amplification and the Polya fitting results.

In recent years, our research has concentrated on experiments involving a 266 nm UV laser [25–28]. We have used its ionization properties to assess the factor f. This method leverages the ionization tracks produced by the UV laser, providing a direct testing approach that minimizes data acquisition times. Furthermore, the laser's exceptional monochromaticity and high stability contribute to the uniformity of ionization clusters along the tracks, thereby enhancing the precision of f measurements. The purpose of this paper is to elucidate the principles and setup of our testing methodology and to present the measurement outcomes for the factor f.

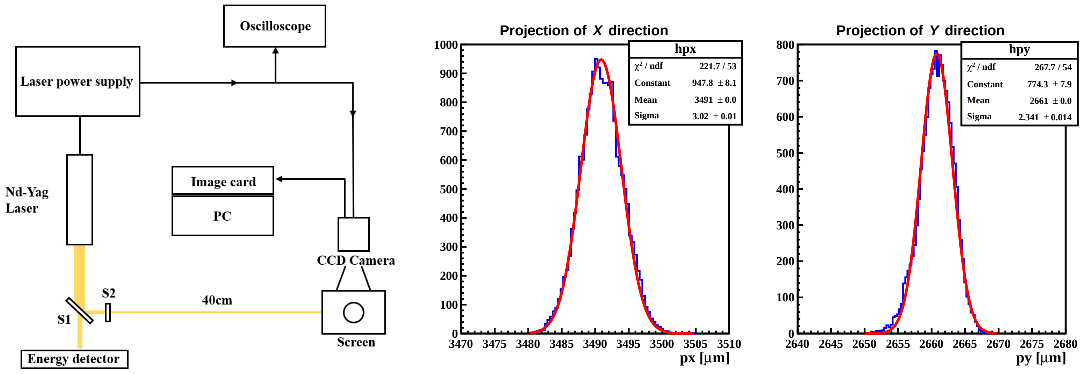

(a) (b)

Fig. 3. (a) The layout of the laser point stability experiment; (b) The fluctuation of the beam spot projected along the X-direction and Y-direction.

II. STABILITY TESTING AND PRINCIPLES OF UV LASER OPERATION

A. Application Mechanisms and Laser Selection

The ionization potential of gases frequently employed in TPCs, such as argon (Ar, 15.7 eV), carbon dioxide (CO_2, 14.4 eV), and methane (CH_4, 13.1 eV), is considerably higher than the photon energy of ultraviolet lasers. Consequently, these lasers cannot ionize the working gas through the photoelectric effect. For example, the photon energy emitted by an N_2 laser with a wavelength of 377 nm is approximately 3.68 eV, while that from a Nd-YAG laser with a wavelength of 266 nm is about 4.68 eV. However, research by Towrie et al. [29] has established that UV lasers can induce ionization of organic impurity gases present in the working gas. These impurities, with their complex energy level structures, primarily undergo two-photon ionization when interacting with UV lasers [30]. Consequently, advanced laser systems have been developed in STAR-TPC [32] and ALICE-TPC [33] to measure and monitor detector performance by creating uniformly distributed laser tracks throughout the detector system [31].

In our experiment, we utilized the Q-smart 100 Nd-YAG laser by Quantel, operating at a wavelength of 266 nm. The laser beam had a diameter of 5 mm and a beam divergence of approximately 0.3 mrad. The signal amplitude of the readout circuit is directly proportional to the laser energy and the size of the laser beam. Gas ionization can be achieved using a UV laser with specific parameters: a gain of 5000, a spot area of 1 mm^2, a 2 mm readout strip, and a preamplifier amplitude of 140 mV [35]. Therefore, for subsequent experiments, we selected a spot area of 1 mm^2 and laser energy of $1 \sim 2\,\mu$J/mm^2.

B. UV Laser Alignment Stability Testing

Temperature fluctuations and vibrations can disrupt beam alignment, leading to drift or jitter. It is essential to conduct quantitative testing to evaluate laser beam alignment stability.

Laser alignment stability is evaluated using a CCD camera, illustrated in Fig. 3(a). S1 and S2 serve as the beam splitter and aperture, respectively, with an aperture size of 1 mm^2. During testing, the laser beam is split by S1, with the transmitted portion monitored by an energy meter, while the reflected portion passes through aperture S2 to form a narrow beam. After traveling 40 cm, the beam is projected onto a screen and continuously captured by a synchronized CCD camera. Over 20 minutes, the camera records the geometric center coordinates of the spot and calculates their average and standard deviation to assess alignment accuracy.

The spot center fluctuation is represented by two Gaussian functions in the X and Y direction, as shown in Fig. 3(b), with standard deviations of about 3.02 μm in the X direction and 2.34 μm in the Y direction. This high stability level ensures precise measurement of the avalanche fluctuation factor.

C. UV Later Energy Stability Testing

In practical applications, variations in the total energy output of laser systems are unavoidable, primarily due to temperature fluctuations that affect crystal performance and the inherent variations in emitted radiative photons during laser operation. For Nd-YAG lasers that utilize frequency-doubling, temperature changes within the system can particularly impact the performance of the frequency-doubling crystal. Although the laser's internal cooling system can partially offset these effects, it is crucial to test the stability of the laser energy to ensure accurate assessments.

To satisfy the experimental demands for microjoule-level laser energy, the energy stability of the attenuated narrow-beam laser was tested using the Ophir energy monitoring system. The testing period lasted 20 minutes, with the results presented in Fig. 4. The test results indicate that the average energy of the low-energy laser after attenuation is 46.59 μJ, with energy stability better than 2.9%. This degree of energy stability meets the requirements for measuring the gain stability factor.

The test results pertain to the energy stability of the UV

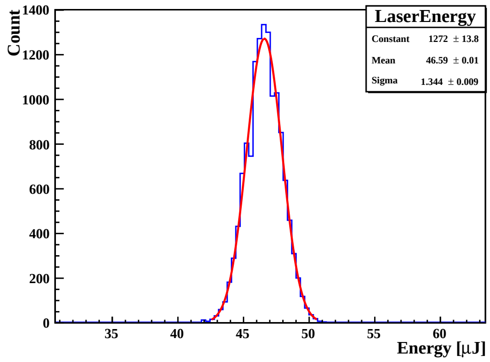

Fig. 4. The results of the UV laser's energy stability during a 20-minute testing duration.

laser over a 20-minute testing period.

III. AVALANCHE FLUCTUATIONS FACTOR TESTING

A. Measurement Principle

As Eq. (2), the effective number of electrons, denoted as N_{eff}, is contingent upon the factor f and the average primary ionization count, N. Employing a 266 nm wavelength laser that operates on a two-photon ionization mechanism, it is possible to generate over 10 million ionized electrons at an energy density of 10 μJ/mm^2. The laser's precise monochromaticity and stability are instrumental in ensuring consistent ionization cluster sizes. Moreover, its ionization capacity can be fine-tuned by adjusting the energy levels to exceed those of minimum ionizing particles, thereby fulfilling the electronic signal requirements. Consequently, with a constant primary ionization, N_{eff} is primarily dependent on the factor f.

Recent studies have demonstrated that the laser ionization energy spectrum adheres to a Gaussian distribution following energy calibration, aligning with the energy distribution of the laser beam itself. The factor f can be determined by comparing the charge signals Q_1 and Q_2, which are collected by adjacent pad rows after the ionized electrons from the laser have been amplified. The theoretical underpinnings of this method are derived from the literature [36, 37].

The total number of amplified electrons, N, collected by a pad row can be represented by Eq. (5):

$$N = \sum_{i=1}^{n} g_i = g_1 + g_2 + \cdots + g_n \tag{5}$$

where n is the total number of primary electrons generated within a pad row's range by laser ionization. g_i is the gain of the i-th electron. The average number and variance of amplified electrons are expressed in Eqs. (6) and (7), respectively:

$$\langle N \rangle = \langle n \rangle \cdot \langle g \rangle \tag{6}$$

$$\begin{aligned} \sigma_N^2 &\equiv \left\langle (N - \langle N \rangle)^2 \right\rangle \\ &= \langle n \rangle \cdot \langle g \rangle^2 \cdot \left(\frac{\sigma_g^2}{\langle n \rangle} + f\right) \end{aligned} \tag{7}$$

The fluctuation in primary ionization is indicated by $\sigma_n^2/\langle n \rangle$ with $\langle n \rangle$ being the average number of primary electrons per laser shot on a pad row. Due to laser stability or drift, there are fluctuations in the measured $\langle n \rangle$, leading to the average $\langle\langle n \rangle\rangle$ over a single experiment's duration, as shown in Eqs. (8) and (9).

$$\langle n \rangle \equiv \langle\langle n \rangle\rangle + \delta\langle n \rangle \tag{8}$$

$$n \equiv \langle\langle n \rangle\rangle + \delta\langle n \rangle + \delta n \tag{9}$$

The average of σ_N^2 during a single experiment can be calculated as Eq. (10):

$$\begin{aligned} \left\langle \sigma_N^2 \right\rangle &\equiv \left\langle (N - \langle\langle N \rangle\rangle)^2 \right\rangle \\ &= \langle\langle n \rangle\rangle \cdot \langle g \rangle^2 \cdot (1 + f) + \langle g \rangle^2 \cdot \left\langle (\delta\langle n \rangle)^2 \right\rangle \end{aligned} \tag{10}$$

where $\langle N \rangle = \langle g \rangle \cdot \langle n \rangle$ represents the average number of amplified electrons gathered by a single readout pad row during the exposure to a single laser pulse. Additionally, $\langle\langle N \rangle\rangle = \langle g \rangle \cdot \langle\langle n \rangle\rangle$ represents the average of $\langle N \rangle$.

Then, the factor f can be obtained by calculating the variance of the number of amplified electrons collected by two nearby pad rows during a single experimental measurement as Eq. (11):

$$\begin{aligned} \left\langle (N_1 - N_2)^2 \right\rangle &= \left\langle ((N_1 - \langle\langle N \rangle\rangle) - (N_2 - \langle\langle N \rangle\rangle))^2 \right\rangle \\ &= 2 \cdot \langle\langle n \rangle\rangle \cdot \langle g \rangle^2 \cdot \left(\frac{\sigma_g^2}{\langle n \rangle} + f\right) \end{aligned} \tag{11}$$

Assuming that the ionization signals collected by two adjacent pad rows are equal, then $\langle N_1 \rangle = \langle N_2 \rangle = \langle N \rangle$, and the fluctuation in laser ionization, $\langle (\sigma_n^2/\langle n \rangle)^2 \rangle$, is eliminated by measuring the charge difference received by nearby pad rows. It follows that:

$$\begin{aligned} \frac{\sigma_n^2}{\langle n \rangle} + f &= \frac{1}{2} \cdot \frac{\left\langle (N_1 - N_2)^2 \right\rangle}{\langle G \rangle^2 \cdot \langle\langle n \rangle\rangle} \\ &= \frac{\langle\langle n \rangle\rangle}{2} \cdot \frac{\left\langle (N_1 - N_2)^2 \right\rangle}{\langle\langle N \rangle\rangle^2} \\ &= \frac{\langle\langle n \rangle\rangle}{2} \cdot \frac{\left\langle (Q_1 - Q_2)^2 \right\rangle}{\langle\langle Q \rangle\rangle^2} \end{aligned} \tag{12}$$

Therefore, the essence of determining the factor f is found in the quantification of two key deviations: the relative fluctuation in primary ionization, denoted as $\sigma_n^2/\langle n \rangle$, and the relative variance in the charge collected by adjacent pad rows, represented by $\langle (Q_1 - Q_2)^2 \rangle$. As a result, forthcoming experiments will focus on precisely measuring these two critical parameters.

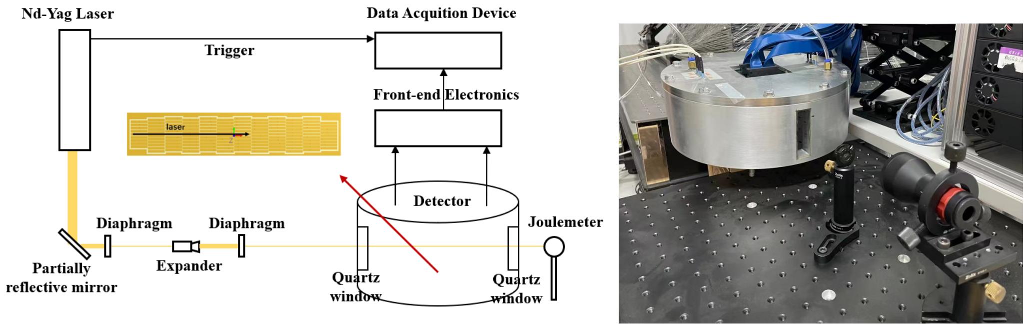

(a) (b)

Fig. 5. (a) Layout of the experimental device; (b) The photo of the detector chamber

B. Experimental setup

The experimental setup is depicted in Fig. 7(a). The laser beam is initially attenuated during the experiment using a 99:1 beam splitter to diminish its energy. Following this, the beam traverses two apertures for collimation, with a beam expander situated between them to refine the beam quality. Once it clears the second aperture, the beam area is expanded to 1 mm^2, and it is then steered into the detector through a quartz glass window, aligning perpendicular to the direction of the electric field, where an energy monitoring system scrutinizes it.

To ensure precise measurements of the laser track, readout pads are centrally positioned within the effective readout area. These pads, which collect electrons along the laser trajectory, consist of 12 rows (a total of 128 pads), with each pad connected to an electronic channel, as depicted in Fig. 7(a). The pad dimensions are 6 mm in length and 1 mm in width. The front-end electronics are based on an ASIC named CASAGEM, which was originally designed for the GEM-TPC [38]. Each ASIC incorporates 16-channel circuits, with an equivalent noise charge (ENC) of less than 2000 for each channel. The gain and shaping time of the ASIC are adjustable, set to 20 mV/fC and 40 ns, respectively, for the experiment. Subsequently, the analog signals are transmitted to a data acquisition (DAQ) system and digitized by a 40 MHz clock [39].

IV. RESULTS

Before commencing laser emission, it is essential to confirm the proper operation of both the DAQ system and the energy monitor. An external trigger signal should be provided to synchronize the measurement of the laser ionization signal with the simultaneous recording of the laser pulse energy. Each data acquisition session spans 40 minutes. To maintain alignment between the laser ionization signal and the laser pulse energy, the laser is turned off before the end of the data collection period.

The experiment initially measured the gain at various voltages across the drift, transfer, and collection regions, as illustrated in Fig.6. At a total voltage differential of 660 V, the gain stands at 800, and it escalates to 7500 at 730 V. For the subsequent experiments, a total voltage differential of 670 V was applied, resulting in a gain of 1040, which aligns with the electronic signal amplitude requirements.

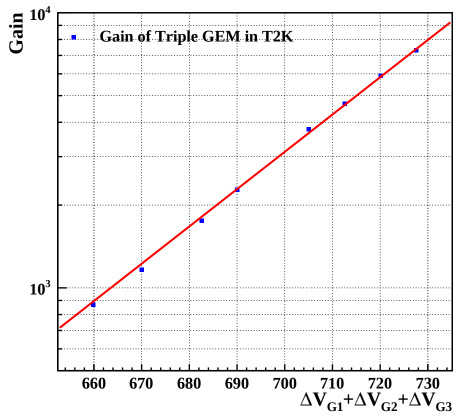

Fig. 6. Gain curve of TripleGEM in T2K Gas.

For the determination of the factor f, it is essential to measure the two key parameters outlined in Eq. (12). It should be noted that the charge Q recorded by the electronics from the pad is directly proportional to N, and $\langle N_1\rangle = \langle N_2\rangle = \langle N\rangle$, therefore $\langle Q_1 - Q_2\rangle = 0$. Consequently, $\langle (Q_1 - Q_2)^2\rangle$ represents the standard deviation of the distribution of the difference in collected charge between adjacent pads. The measurement of $\sigma_n^2/\langle n\rangle$ is derived from measuring the average primary ionization of the laser on the pad row, as depicted in Fig. 5(a). The mean and standard deviation of the fitting result correspond to $\langle n\rangle$ and σ_n respectively. The relationship between Q and n is converted through the gain of the detector. Regarding the second parameter, $\langle (Q_1 - Q_2)^2\rangle$, it involves a statistical calculation of the ratio of the difference in collected charge near the pad to the average collected charge. The statistical outcomes are then plotted into a histogram to determine the standard deviation of the fitted distribution.

A parameter P can be defined by:

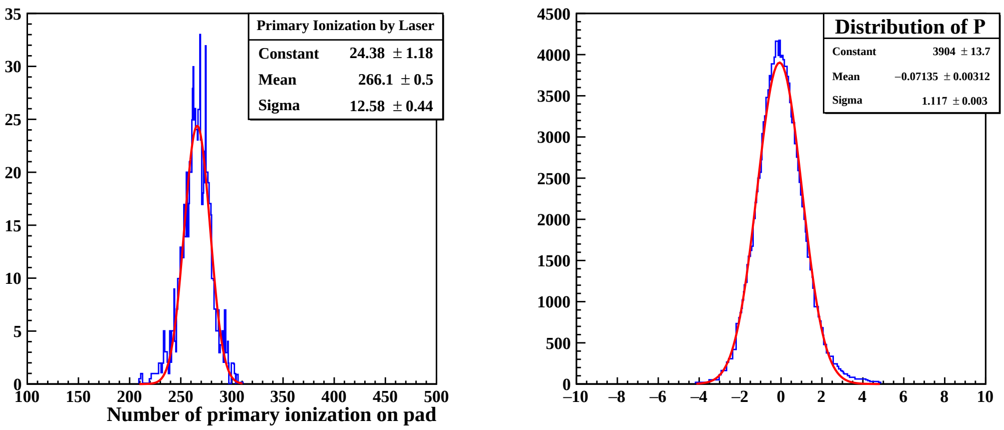

(a) (b)

Fig. 7. (a) The average primary ionization of the UV laser on the readout pad; (b) Distribution of parameter P.

$$P = \sqrt{\frac{\langle n \rangle}{2} \cdot \frac{\langle Q_1 - Q_2 \rangle}{\langle Q \rangle}} \tag{13}$$

Then,

$$\begin{aligned} f &= \frac{\langle\langle n \rangle\rangle}{2} \cdot \frac{\langle (Q_1 - Q_2)^2 \rangle}{\langle\langle Q \rangle\rangle} - \frac{{\sigma_n}^2}{\langle n \rangle} \\ &= {\sigma_P}^2 - \frac{{\sigma_n}^2}{\langle n \rangle} \\ &= 0.65 \pm 0.047 \end{aligned}$$

The experimental findings revealed an avalanche fluctuation factor of 0.65 at a gain of approximately 1040, which closely aligns with the simulated result of 0.66 at the same gain, thereby confirming the reliability of the experimental procedure. This result is consistent with the outcomes of the KEK experiment conducted in 2017, which reported f values of 0.65 and 0.62 at gains of 1900 and 5800, respectively. Furthermore, the number of average primary ionization electrons on the pad row, as shown in Fig. 5(a), was determined to be $N = 266.1$. Employing Eq. (2), the number of effective electrons was estimated to be $N_{eff} = 160.8$. Consequently, adjusting the laser energy to modify the size of N in subsequent experiments may result in a higher N_{eff}, which could subsequently enhance the position resolution of the laser in TPC applications.

V. CONCLUSION

This study utilized a Triple-GEM cascaded amplification structure to investigate the avalanche fluctuation factor f using UV laser ionization tracks. At a gain of 1040, we achieved $f = 0.65$ which is in agreement with the testing conclusions from KEK. This method is simpler than traditional approaches, demands lower electronic noise, and exhibits higher repeatability. To ensure the stability of the UV laser, we conducted tests on its pointing and energy stability. The results indicated that the energy stability of the attenuated low-energy narrow-beam laser is better than 2.9%. The laser alignment stability in the X and Y dimensions was measured at 3.02 μm and 2.34 μm. Furthermore, the accurate measurement of the avalanche fluctuation factor enables the estimation of the number of effective electron N_{eff}. By adjusting the laser energy, a larger N_{eff} value can be achieved, thereby enhancing the laser's ultra-high position resolution. Consequently, the laser shows considerable potential in high-precision TPC research.

VI. ACKNOWLEDGEMENTS

The author expresses gratitude to Professor Yulan Li and Dr. Zhiyang Yuan for their insightful discussions. This research was funded by the National Key Research and Development Program (Grant No. 2016YFA0400400), the National Natural Science Foundation of China (Grant No. 11975256), and the National Natural Science Foundation of China (Grant No. 11535007).

VII. BIBLIOGRAPHY

[1] D. Attie, TPC review. Nucl. Instrum. Meth. A **598**, 89-93 (2009). doi: 10.1016/j.nima.2008.08.114

[2] H. K. Wu, X. Y. Wang, Y. M. Wang *et al.*, Fudan multi-purpose active target time projection chamber (fMeta-TPC) for pho-

tonuclear reaction experiments. Nucl. Sci. Tech. **35** 200 (2024). doi: 10.1007/s41365-024-01576-1

[3] L.S. Yang, J.Y. Xu, Q.T. Li *et al.*, Performance of the CAT-TPC based on two-dimensional readout strips. Nucl. Sci. Tech. **32**, 85 (2021). doi: 10.1007/s41365-021-00919-6

[4] X. G. Cao, Y. L. Chang, K. Chen *et al.*, NvDEx-100 conceptual design report. Nucl. Sci. Tech. **35**, 3 (2024). doi: 10.1007/s41365-023-01360-7

[5] K.X. Ni, Y.H. Lai, A. Abdukerim *et al.*, Searching for neutrinoless double beta decay of ^{136}Xe with PandaX-II liquid xenon detector. Chin. Phys. C **43**, 113001 (2019). doi: 10.1088/1674-1137/43/11/113001

[6] D. M. Asner, T. Barklow, C. Calancha *et al.*, ILC Higgs white paper. Community Summer Study 2013 : Snowmass on the Mississippi, MN, USA, 29 Jul - 6 Aug 2013. doi: 10.48550/arXiv.1310.0763

[7] F. F. An, Y. Bai, C. H. Chen *et al.*, Precision Higgs physics at the CEPC. Chin. Phys. C **43**, 043002 (2019). doi: 10.1016/j.nima.2008.08.114

[8] H. Cheng, W.H. Chiu, Y. Fang *et al.*, The physics potential of the CEPC. Prepared for the US Snowmass community planning exercise (Snowmass 2021) (2022). doi: 10.48550/arXiv.2205.08553

[9] Z. X. Chen, Y. Yang, M.Q. Ruan *et al.*, Cross section and higgs mass measurement with higgsstrahlung at the CEPC. Chin. Phys. C **41** 023003 (2017). doi: 10.1088/1674-1137/41/2/023003

[10] M. Zhao, M.Q. Ruan, H. R. Qi *et al.*, Feasibility study of TPC at electron positron colliders at Z pole operation. J. Instrum **12** 07005 (2017). doi: 10.1088/1748-0221/12/07/P07005

[11] R. Diener, LCTPC collaboration, Development of a TPC for an ILC Detector. Physcs Proc **37**, 456-463 (2012). doi: 10.1016/j.phpro.2012.02.393

[12] M. Kobayashi, R. Yonamine, T. Tomioka *et al.*, Cosmic ray tests of a GEM-based TPC prototype operated in Ar–CF4–isobutane gas mixtures. Nucl. Instrum. Meth. A **641**, 37-47 (2011). doi: 10.1016/j.nima.2011.02.042

[13] F. Sauli, GEM: A new concept for electron amplification in gas detectors.Nucl. Instrum. Meth. A **386**, 531-534 (1997). doi: 10.1016/S0168-9002(96)01172-2

[14] Y. Wang, L. Zhang, A. Jung *et al.*, Simulation study of the performance of quadruple-GEM detectors. Radiat. Detect. Technol. Methods **7**, 107–116 (2023). doi: 10.1007/s41605-022-00361-1

[15] T. Alexopoulos, A.A. Altintas, M. Alviggi *et al.*, Development of large size Micromegas detector for the upgrade of the ATLAS Muon system. Nucl. Instrum. Meth. A **617**, 161-165 (2010). doi: 10.1016/j.nima.2009.06.113

[16] H. Y. Du, C.B. Du, K.Giboni *et al.*, Screener3D: a gaseous time projection chamber for ultra-low radioactive material screening. Nucl. Sci. Tech **32**, 142 (2021). doi: 10.1007/s41365-021-00983-y

[17] H. Ito, T. Hashimoto, K. Miuchi *et al.*, Development of an alpha-particle imaging detector based on a low radioactive micro-time-projection chamber. Nucl. Instrum. Meth. A **953**, 163050 (2020). doi:10.1016/j.nima.2019.163050

[18] M Kobayashi, An estimation of the effective number of electrons contributing to the coordinate measurement with a TPC: II. Nucl. Instrum. Meth. A **729**, 161-165 (2013). doi: 10.1016/j.nima.2013.07.028

[19] T. Zerguerras, B. Genolini, F. Kuger *et al.*, Understanding avalanches in a Micromegas from single-electron response measurement. Nucl. Instrum. Meth. A **772**, 76-82 (2015). doi: 10.1016/j.nima.2014.11.014

[20] Y Meng, Z Wang, Y Yao *et al.*, Dark Matter Search Results from the PandaX-4T Commissioning Run. Phys. Rev. Lett **127**, 261802 (2021). doi: 10.1103/PhysRevLett.127.261802

[21] X. Chen, C. B. Fu, J. Galan *et al.*, PandaX-III: Searching for neutrinoless double beta decay with high pressure 136Xe gas time projection chambers. Sci. China Phys. Mech. Astron. **60**(6), 061011 (2017). doi: 10.1007/s11433-017-9028-0

[22] T. Zerguerras, B. Genolini, V. Lepeltier *et al.*, Single-electron response and energy resolution of a Micromegas detector. Nucl. Instrum. Meth. A **608**, 397-402 (2009). doi: 10.1016/j.nima.2009.07.015

[23] I. COMSOL, COMSOL Multiphysics 5.5 User's Guide (2020). https://www.comsol.com/

[24] H. Schindler, Garfield++ user's guide (2023). https://garfieldpp.web.cern.ch/garfieldpp/

[25] Y. L. Zhang, H. R. Qi, B. T. Hu *et al.*, A hybrid structure gaseous detector for ion backflow suppression. Chin. Phys. C **41**(5), 056003 (2017).doi: 10.1088/1674-1137/41/5/056003

[26] H. Y. Wang, H. R. Qi, Design and study of the TPC detector module and prototype for CEPC. INT J MOD PHYS A. **34**, 1940016 (2019). doi.org/10.1142/S0217751X19400165

[27] Y. M. Cai, H. R. Qi, L. Liu *et al.*, Investigation of UV laser ionization in argon-based gas mixtures with a Triple-GEM detector. J. Instrum **15**, T02001 (2020). doi: 10.1088/1748-0221/15/02/T02001

[28] Z. Y. Yuan, H. R. Qi, Y. Chang *et al.*, Performance of TPC detector prototype integrated with UV laser tracks for the circular collider. Nucl. Instrum. Meth. A **1040**, 167241 (2022). doi: 10.1016/j.nima.2022.167241

[29] M Towrie, J W Cahill, K W D Ledingham *et al.*, Detection of phenol in proportional-counter gas by two-photon ionisation spectroscopy. J. Phys. B-AT. Mol. Opt **19**, 13 (1989). doi: 10.1088/0022-3700/19/13/010

[30] S. Drysdale, K. Ledingham, C. Raine *et al.*,Detection of toluene in a proportional counter gas by resonant two photon ionisation spectroscopy. Nucl. Instrum. Meth. A **252**, 521-523 (1986). doi: 10.1016/0168-9002(86)91234-9

[31] H. J. Hilke, Detector calibration with lasers—A review. Nucl. Instrum. Meth. A **252**, 169-179 (1986). doi: 10.1016/0168-9002(86)91177-0

[32] K. H. Ackermann, N. Adams, C. Adler *et al.*, STAR detector overview. Nucl. Instrum. Meth. A **499**, 624-632 (2003). doi: 10.1016/S0168-9002(02)01960-5

[33] J. Alme, Y. Andres, H. Appelshäuser *et al.*, The ALICE TPC, a large 3-dimensional tracking device with fast readout for ultra-high multiplicity events. Nucl. Instrum. Meth. A **622**, 316-367 (2010). doi: 10.1016/j.nima.2010.04.042

[34] P. Gasik, Development of GEM-based Read-Out Chambers for the upgrade of the ALICE TPC. J. Instrum **9**, 04035 (2014). doi: 10.1088/1748-0221/9/04/C04035

[35] H. Y. Wang, H. R. Qi, L. Liu *et al.*, Signal and pointing accuracy of ultraviolet laser in micro-pattern gaseous detector. Acta. Phys. Sin. **68**, 022901 (2019). WLXB.0.2019-02-007

[36] M. Kobayashi, T.Ogawa, T.Kawaguchi *et al.*, A novel technique for the measurement of the avalanche fluctuation of gaseous detectors. Nucl. Instrum. Meth. A **845**, 236-240 (2017). doi: 10.1016/j.nima.2016.06.073

[37] M. Kobayashi, K. Yumino, T. Ogawa *et al.*, Detectors and Associated Equipment. Nucl. Instrum. Meth. A **1039**, 166872 (2022). doi: doi.org/10.1016/j.nima.2022.166872

[38] L. He, Z. Deng, Y. N. Liu *et al.*, Development of a multi-channel readout ASIC for a fast neutron spectrometer

based on GEM-TPC. Chin. Phys. C **38**, 106101 (2014). doi: doi.org/10.1088/1674-1137/38/10/106101

[39] Y. Huang, H. Gong, J. Li *et al.*, Development of the readout system for a time projection chamber prototype. J. Instrum **14**, T01001 (2019). doi: doi.org/10.1088/1674-1137/38/10/106101